Journal of Nuclear Medicine, published on March 24, 2022 as doi:10.2967/jnumed.121.263674

Title

Factors for differential outcome across cancers in clinical molecular-targeted fluorescence imaging

Authors

Quan Zhou[1,2,*], Nynke S. van den Berg[2], Wenying Kang[2], Jacqueline Pei[2], Naoki Nishio[2,3], Stan van Keulen[2,4], Myrthe A. Engelen[2,5], Yu-Jin Lee[2], Marisa Hom[2], Johana C. M. Vega Leonel[1], Zachary Hart[2], Hannes Vogel[6], Romain Cayrol[6], Brock A. Martin[6], Mark Roesner[7], Glenn Shields[7], Natalie Lui[8], Melanie Hayden Gephart[1], Roan C. Raymundo[2,9], Grace Yi[2,9], Monica Granucci[9], Gerald A. Grant[1], Gordon Li[1], Eben L. Rosenthal[2,7,*]

Affiliations

[1] Department of Neurosurgery, Stanford University School of Medicine, Stanford, CA, USA

[2] Department of Otolaryngology, Stanford University School of Medicine, Stanford, CA, USA

[3] Department of Otorhinolaryngology, Nagoya University Graduate School of Medicine, Nagoya, Japan

[4] Department of Oral and Maxillofacial Surgery and Oral Pathology, Amsterdam UMC-location VUMC/Academic Centre for Dentistry Amsterdam (ACTA), Amsterdam, The Netherlands

[5] Department of Mechanical Engineering, Delft University of Technology, Delft, Netherlands

[6] Department of Pathology, Stanford University, Stanford, CA, USA

[7] Stanford Health Care, Stanford University Medical Center, Stanford, CA, USA

[8] Department of Cardiothoracic Surgery, Stanford University Medical Center, Stanford, CA, USA

[9] Cancer Clinical Trials Office, Stanford University School of Medicine, Stanford, CA, USA

Disclosure

E.L.R. acts as consultant for LI-COR Biosciences Inc. and has equipment loans from this company. All other authors declare no conflict of interest.

*Correspondence to:

Quan Zhou, PhD
Postdoctoral Fellow
Departments of Otolaryngology and Neurosurgery
Stanford University
1201 Welch road MSLS P329
Stanford, CA 94305
Tel: 650-726-6034 | Fax: 650-736-8100
ORCID ID: 0000-0002-9351-5614
Email: qzh@stanford.edu

Eben L. Rosenthal, MD
Department of Otolaryngology-Head and Neck Surgery
Vanderbilt University Medical Center
1215 21st Ave. S. Suite 6310
Medical Center East, South Tower
Nashville, TN 37232
Phone: 615-936-0708 | Fax: 615-936-0704
Email: e.rosenthal@vumc.org

Word count

5000

Running title

Factors for molecular imaging outcome

ABSTRACT

Clinical imaging performance using a fluorescent antibody was compared across three cancers to elucidate physical and biological factors contributing to differential translation of epidermal growth factor receptor (EGFR) expression to macroscopic fluorescence in tumors.

Methods

Thirty-one patients with high-grade glioma (HGG, n = 5), head-and-neck squamous cell carcinoma (HNSCC, n = 23) or lung adenocarcinoma (LAC, n = 3) were systemically infused with 50 mg panitumumab-IRDye800, 1 – 3 days prior to surgery. Intraoperative open-field fluorescent images of the surgical field were acquired, where imaging device settings and operating room lighting conditions were tested on tissue-mimicking phantoms. Fluorescence contrast and margin size were measured on resected specimen surface. Antibody distribution and EGFR immunoreactivity were characterized in macroscopic and microscopic histological structures. Integrity of the blood-brain barrier (BBB) was examined via tight junction protein (claudin-5) expression with immunohistochemistry. Stepwise multivariate linear regression of biological variables was performed to identify independent predictors of panitumumab-IRDye800 concentration in tissue.

Results

Optimally acquired at the lowest gain for tumor detection with ambient light, intraoperative fluorescence imaging enhanced tissue-size dependent tumor contrast by 5.2-fold, 3.4-fold and 1.4-fold in HGG, HNSCC and LAC, respectively. Tissue surface fluorescence target-to-background ratio correlated with margin size and identified 78 – 97% of at-risk resection margins *ex vivo*. In 4 μm-thick tissue sections, fluorescence detected tumor with 0.85 – 0.89 areas under the receiver operating characteristic curves. Preferential breakdown of BBB in HGG improved tumor specificity of intratumoral antibody distribution relative to that of EGFR (96% vs 80%) despite its reduced concentration (3.9 ng/mg tissue) compared to HNSCC (8.1 ng/mg) and LAC (6.3 ng/mg). Cellular EGFR expression, tumor cell density, plasma antibody concentration

and delivery barrier were independently associated with local intratumoral panitumumab-IRDye800 concentration with 0.62 goodness-of-fit of prediction.

Conclusions

In multi-cancer clinical imaging of receptor-ligand based molecular probe, plasma antibody concentration, delivery barrier, as well as intratumoral EGFR expression driven by cellular biomarker expression and tumor cell density, led to heterogeneous intratumoral antibody accumulation and spatial distribution while tumor size, resection margin, and intraoperative imaging settings substantially influenced macroscopic tumor contrast.

Key words

Clinical fluorescence imaging, epidermal growth factor receptor, multi-cancer surgical imaging, physical and biological factors, panitumumab-IRDye800

INTRODUCTION

Intraoperative surgical imaging with tumor-specific fluorescent tracers offers additional tumor contrast for surgeons, who rely heavily on visual cues for resection decisions. In recent years, receptor-ligand based imaging probes have achieved early successes in detecting cancers of the head-and-neck, brain, ovary, pancreas, kidney, prostate and colon (*1-7*). Yet how biomarker expression translates to fluorescence and clinical imaging outcome remains unexamined. As more molecular imaging probes enter late phase clinical trials, we compared the performance of a fluorescently labeled epidermal growth factor receptor (EGFR) antibody, panitumumab-IRDye800, in different tumor types to elucidate intrinsic and extrinsic parameters that influence tumor imaging and inform clinical decisions.

Our primary objective was to examine, in multiple cancers, physical and biological factors that contributed to differential fluorescence imaging outcome in terms of intraoperative tumor contrast, pathological margin assessment and fluorescent antibody distribution. Various combinations of biomarker targets, molecular probes, imaging devices and analysis methods among imaging studies make collective interpretation of their findings challenging. For trials with dose escalation design, results between cohorts can be naturally reported within the same analysis framework as illustrated in breast cancer (*8*). However, no consensus exists yet to evaluate a molecular probe among multiple cancers. We therefore acquired and processed fluorescence images across malignancies with the same imaging and analysis pipeline to identify attributes that bridge the gap between molecular characteristics and imaging outcome in fluorescence-guided surgery.

MATERIALS AND METHODS

Participants

Open-label phase I/II clinical trials (NCT03510208, NCT02415881 and NCT03582124) were conducted in adult patients undergoing surgical resection at Stanford Hospital for high-grade glioma (HGG, n = 5), head-and-neck squamous cell carcinoma (HNSCC, n = 25) and lung adenocarcinoma (LAC, n = 3), respectively.

Between Aug 2017 and Nov 2019, 33 enrolled patients received a single dose of 50 mg panitumumab-IRDye800 (produced following current Good Manufacturing Practices by the Frederick National Laboratory, Frederick, MD, USA) regardless of weight or gender 1 – 3 days prior to surgery. Adverse events were collected up to 30 days after infusion. Two HNSCC patients were excluded from final analysis as no cancer was found in their resected tissue. Maximum dimension of tumor size was determined by pre-surgical magnetic resonance imaging or computed tomography. Areas of viable tumor as well as normal tissue were outlined by board-certified pathologists on representative histology staining of tissue sections. Institutional Review Board approved this study and all subjects signed a written informed consent.

Fluorescence imaging

As illustrated in tissue processing and imaging workflow (Figure 1), a laparoscope or a handheld camera attached to the SPY fluorescence imaging platform (Novadaq) detected intraoperative NIR fluorescence of the tumor and wound bed. Intraoperative blood samples were collected to measure plasma panitumumab-IRDye800 concentration. Solid tumors were resected en bloc while diffuse HGGs were removed in pieces. *Ex vivo* fresh tissue was imaged in Pearl Trilogy Imaging System (LI-COR Biosciences) without ambient light. Solid tumors were fixed and sectioned into 5 mm-thick serial cross sections and paraffin embedded in tissue blocks. Histological and immunohistochemical stainings were performed on 4 μm-thick tissue sections. Fluorescence images of both tissue blocks and sections were acquired in Odyssey CLx scanner (LI-COR). The distance from the tissue resection surface to solid tumor margin was measured on histology sections.

Fluorescence quantification

Tumor contrast was measured by the ratio of average pixel intensities (ImageJ 1.53c (*9*)) from five circular regions of interest (ROIs, d = 20 pixels, x, y coordinates determined from randomly generated integer pairs) inside tumor and surrounding normal areas in intraoperative white light and fluorescence images. Fluorescence histograms were plotted for the entire tumor and peritumoral normal areas. High-intensity

peaks in the fluorescence map of resected tissue were isolated as previously described (*10*). Mean fluorescence intensity (MFI) was measured in Image Studio (LI-COR) as total fluorescence signal divided by the pixel number within ROIs. MFI in normal tissue was measured in muscle or brain tissue with < 20% tumor cells. Tumor-to-background ratio (TBR) on fresh resected tissue surface denoted the ratio of MFIs in circular ROIs (d = 2 mm) over tumor versus those over normal tissue. TBR of tissue sections was the ratio of MFI within outlined tumor versus uninvolved tissue. Fluorescence heterogeneity denoted the standard deviation of fluorescence signal normalized by MFI. MFIs of anatomic structures (circular ROIs, d = 200 μm) on tissue sections were measured.

Tissue-mimicking phantoms

Serial dilutions of panitumumab-IRDye800 (0 – 10.0 g/mL) were respectively dissolved in 1% agarose (Life Technologies) and 1% intralipid (Sigma-Aldrich) at 45°C and poured into 200 μL cylindrical molds. Solidified phantoms were imaged (SPY platform, gain: 2, 4 and 8) in the operating room under three lighting conditions (ambient lights: TL-D, 36W, Philips; room lights: A19, 100W, Osram; overhead lights: F528, 140W, Stryker). The ratio of MFIs between panitumumab-IRDye800 and saline containing phantoms measured imaging contrast. Phantom MFIs measured in Pearl and Odyssey were correlated. Panitumumab-IRDye800 concentrations and MFIs of 4 μm phantom sections were fitted by polynomial regression.

Immunohistochemistry

EGFR (RM-2111-RQ, Thermo Fisher Scientific; secondary: SM805, Agilent Technologies) immunohistochemistry and hematoxylin counterstaining were performed after heat mediated antigen retrieval with Dako Autostainer (Agilent) along positive and negative controls. Double immunohistochemical staining of Claudin-5 (1:500, 34-1600, Thermo Fisher) and ETS-related gene (ERG, 1:1000, EPR3864, Abcam) was performed on HGG tissue to assess blood-brain barrier (BBB) integrity (*2*). Immunoreactivity was visualized with diaminobenzidine (for EGFR and Claudin-5) and magenta (for ERG) chromogens (Dako), and scanned in NanoZoomer 2.0-HT (Hamamatsu Photonics). The percentage of

pixels with moderate to strong staining was quantified with ImageScope (Aperio Technologies) as previously described (*11*). EGFR+ tumor cells within tumor outlines were counted with a MATLAB algorithm.

Statistical analysis

Group statistics were expressed as mean ± standard error unless specified otherwise. Patient characteristics were compared between cancer types using analysis of variance (ANOVA) and Pearson's Chi-square tests as appropriate. Paired t-tests (two-tailed) were performed for group comparisons between tumor and normal tissues in each cancer type. One-way ANOVA was performed for group comparisons among trials. Whiskers and outliers of box plots were determined by the Tukey method. Receiver operating characteristics (ROC) curves were plotted for distinguishing histological tumor versus normal tissue using MFI and EGFR%, respectively. Sensitivity, specificity, area under the ROC curve (AUC), negative and positive predictive values were subsequently calculated using these definitions. MFI and EGFR% cutoff values that resulted in the maximal sensitivity and specificity combined were reported. Biological variables were included in a stepwise multivariate linear regression model to identify independent predictors of local panitumumab-IRDye800 concentration. To exclude the possibility of false-positive associations, multicollinearity of predictors was assessed using the variance inflation factor (VIF), and predictors with VIF > 5 were removed from the final model. Significance was defined at *$P < 0.05$; ** $P < 0.01$; *** $P < 0.001$; **** $P < 0.0001$.

RESULTS

Clinical data

No significant difference was found between trials in demographic features, weight-adjusted tracer dose, plasma panitumumab-IRDye800 concentration and imaging window, Table 1. While tumor size was similar among trials ($P = 0.35$), resected tissue size varied significantly between diffuse HGGs removed in pieces

and solid tumors resected en bloc (16% ± 4% vs. 184% ± 20% of the tumor size, $P = 0.0002$), Supplemental Figure 1. No infusion reactions or dose limiting toxicity events occurred, Supplemental Table 1.

Intraoperative tumor visualization

Intraoperative fluorescence was diffuse in LAC compared to the strong signal in HGG and HNSCC that allowed distinct separation of disease tissue from normal areas based on histological confirmation, with notable heterogeneity in HGG, Figure 2A. Minimal fluorescence remained in the wound beds of HNSCC and LAC, while fluorescent residual HGG involving eloquent cortex located beyond contrast-enhancing margin was not removed in the resection cavity, Supplemental Fig. 2. NIR imaging enhanced tumor contrasts relative to white light illumination by 5.2 ($P = 0.0006$), 3.4 ($P < 0.0001$) and 1.4 ($P = 0.03$) folds for HGG, HNSCC and LAC, respectively, and fluorescence contrasts dropped below 1.0 in the wound beds Supplemental Fig. 3. *Ex vivo* tissue fluorescence contrast correlated with resected tumor size ($P = 0.007$), Supplemental Fig. 4.

The open-field fluorescence imaging had limited sensitivity and dynamic range over tissue-mimicking phantoms containing panitumumab-IRDye800, which were readily distinguished from each other without ambient light, Fig. 2B. Per workflow requirements, ambient lighting was always present in the operating room. Detection sensitivity was improved with higher gain (blue vs. yellow circles), at the cost of reduced saturation threshold (pink vs red circles). Operating room lights gave false positive signals and images of control phantoms were saturated with overhead lights, indicating NIR interference from these light sources.

Margin assessment

Fluorescence intensity peaks on fluorescence images of resected tumor specimens identified at-risk margin, Figure 3A. The HGG cell density decreased beyond the infiltrating edge, and distances from tissue surface to tumor margin were inversely correlated with fluorescence contrast on specimen surface, Fig. 3B. Positive and close margins can be captured above the target-to-background value at 5 mm on fitted regression curves

with 97% and 78% detection rates for HNSCC and LAC, respectively, while 93% HGG infiltrative edges with ≥ 50% tumor cell density were detected.

Intratumoral fluorescent antibody distribution

Microscopic NIR images of tissue blocks and sections exposing tumor interior confirmed intratumoral distribution and cellular delivery of panitumumab-IRDye800, Figure 4A. Fluorescence heterogeneity in HGG were more pronounced than in LAC (P = 0.02) with similar tumoral fluorescence contrast across cancers, Fig. S5. Fluorescence in tissue sections can effectively distinguish tumor against normal tissue (AUC: HNSCC > LAC > HGG = 0.85, Supplemental Fig. 6). Differences in tumor fluorescence converged from 244 to 21 folds (Supplemental Fig. 7) as variance in tissue thickness reduced from centimeters in fresh tissue to < 1 μm in tissue sections, while their fluorescence intensity measurements by two closed-field devices were correlated, Supplemental Fig. 8.

Panitumumab-IRDye800 concentration (inferred from fluorescence, Supplemental Fig. 9) were higher inside tumoral outlines relative to healthy adjacent tissue of HGG (3.9 vs 1.6 ng/mg, P < 0.0001), HNSCC (8.1 vs 3.9 ng/mg, P < 0.0001) and LAC (6.3 vs 4.5 ng/mg, P = 0.0006), Fig. 4B. Further delineation into finer histological structures revealed greater probe distribution in microscopic LAC tumor nodules relative to macroscopic tumoral area, indicating substantial presence of stroma with low antibody delivery inside LAC. Likely due to its EGFR expression, head-and-neck mucus exhibited distinctly high probe uptake among non-tumoral areas including normal (muscle, lung and brain) tissue, lymph node, stroma, fat, and necrosis.

Biomarker expression and tumor cell density

EGFR expression was heterogeneous, Figure 5A, with greater fidelity for tumor presence in HNSCC and HGG than LAC (AUCs = 0.96 and 0.94 vs 0.82), Supplemental Fig. 10. Non-specific delivery to peritumoral EGFR negative regions, however, was observed in head-and-neck as well as lung tissue (Fig. 4A & 5A). Higher total tumoral EGFR expression translated to greater panitumumab-IRDye800

concentration in tumors with the notable exception of HGG (Fig. 4B & 5A), indicating delivery barrier confirmed by IHC assessment of BBB integrity via tight junction protein, claudin-5, Supplemental Fig. 11. EGFR-positive HGG cells were diffuse while focal clusters of HNSCC and LAC were dispersed among EGFR-negative stroma and fibroblast tissue, Fig. 5B.

The interplay of cellular expression, tumor cell density and distribution pattern led to the scale-dependent nature of EGFR expression. Cellular EGFR level was particularly high in HGG (80% vs. 64% in HNSCC and 60% in LAC, $P = 0.0005$ and 0.001, respectively), but similar between HNSCC and LAC ($P = 0.8$). EGFR+ tumor cells (Fig. 5C) were dense in HGG (3000 ± 450 cells/mm^2) and HNSCC (2100 ± 180 cells/mm^2), but sporadic in LAC (1300 ± 100 cells/mm^2) with fewer than 10 cells occupying over 50% of tumor areas, Supplemental Fig. 12. EGFR immunoreactivity thus varied with magnification powers and specific intratumoral locations examined, Supplemental Fig. 13.

Multivariate analysis

In stepwise multiple linear regression analysis (insignificant independent variables removed one by one) controlled for other significant covariates such as tissue thickness, four biological factors (Table 2) including tumor cell density ($P = 0.015$), cellular EGFR expression% ($P = 0.002$), panitumumab-IRDye800 plasma concentration ($P < 0.0001$) and absence of delivery barrier ($P < 0.0001$), were independently associated (VIF = 1.08, 1.15, 1.16 and 1.08, respectively) with local intratumoral panitumumab-IRDye800 concentration (goodness-of-fit: 0.62, Figure 6).

DISCUSSION

In a receptor-ligand based fluorescence imaging framework encompassing three cancers, we identified various factors that contributed to how biomarker expression translated to clinically relevant tumor imaging outcomes in terms of tumor contrast enhancement, at-risk margin detection and fluorescent antibody distribution. While cellular EGFR expression, tumor cell density, plasma antibody concentration and delivery barrier may predict fluorescent antibody distribution in tissue, operating room lighting, imaging

device settings, tumor size and depth can substantially alter the intraoperative fluorescent tumor contrast at specific locations on the tissue surface of each particular patient. The interplay of these intrinsic and extrinsic attributes determined the differential translation of cellular biomarker expression to antibody uptake in tissue and ultimately the disparity in macroscopic fluorescent tumor contrast, with respective implications for projecting therapeutic antibody delivery and implementing surgical fluorescence imaging.

Physical imaging conditions and biological tissue properties were isolated through the imaging and analysis pipeline. In particular, *ex vivo* closed-field fluorescence imaging eliminated ambient light and standardized acquisition settings that affected intraoperative open-field images. Similarly, in 4 μm-thick tumor cross sections, overlaying normal tissue of resected whole tissue specimens was removed and variable thickness of tumor tissue along the imaging path was equalized. In these optically transparent thin tissue sections, difference in light scattering properties among tumor types was negligible to allow accurate quantification of fluorescence-based antibody distribution and antigen expression at microscopic resolution, revealing delivery barrier and tumor cell density as molecular and cellular underpinnings of their corresponding macroscopic characteristics.

To accommodate the wide range of inter-patient fluorescence signal, minimal ambient light and the lowest imaging gain allowing tumor detection via fluorescence are recommended to maximize tumor-specific visual contrast in open-field intraoperative imaging, extending findings from previous phantom studies (*12,13*). While only a few fluorescence peaks were sampled for pathological assessment of head-and-neck cancer in previous studies (*10,14*), tissue surface fluorescent contrast was comprehensively characterized against margin distance in our study to identify TBR cutoff values for detecting positive and close resection margins across three malignancies. In addition, rather than quantifying drug concentrations from tissue homogenate (*15*), we mapped antibody distribution to microscopic anatomical structures with high resolution (21 μm) and ultra-sensitivity (2 picograms of tissue) via fluorescence from intact tumor sections, preserving tissue integrity for downstream immunohistochemistry assays.

Our EGFR immunohistochemistry results revealed the scale-dependent and multi-factorial nature of biomarker expression, reflecting its intrinsic intra-tumoral and inter-patient heterogeneity across cancers. The Human Protein Atlas comparing EGFR expression among 20 cancer types reported moderate to strong immunoreactivity in 75% of patients with malignant glioma or head-and-neck cancer, followed by 64% of lung cancer patients (*16*). In the current study, total tumoral EGFR expression correlated with intratumoral antibody concentration, fluorescence and tumor contrast, except for HGG which had the highest total EGFR expression (89%, followed by HNSCC: 62% and LAC: 41%) yet received less than half the panitumumab-IRDye800 delivery observed in HNSCC (3.9 vs. 8.1 ng/mg), suggesting delivery barrier which was confirmed by immunohistochemical staining of tight junction protein.

The preferential intratumoral BBB breakdown by HGG promoted the tumor specificity of antibody distribution beyond that of the molecular target itself, despite introducing greater heterogeneity in fluorescence. Reduced tight junction protein expression around blood vessels indicated compromised BBB integrity in viable glioma tissue. Accordingly, specific cellular fluorescence confirmed panitumumab-IRDye800 delivery across leaky blood-tumor barrier, while intact BBB in normal brain tissue ensured minimal antibody delivery despite substantial EGFR expression, resulting in improved fluorescent tumor contrast consistent with prior preclinical (*17*) and clinical (*2,18,19*) evidence that even modest EGFR expression was sufficient for HGG detection with panitumumab-IRDye800.

In these early phase clinical studies designed for safety and feasibility assessment, representation of certain populations was lacking and fluorescence was not used for intraoperative decision making per IRB protocols, while its tumor specificity warrants further efficacy studies in later stage trials. Intraoperative wound bed imaging was more valuable for piece-wise glioma resection (*2,20*) than solid tumor removed en bloc with negative margin. Due to the dose-dependent nature of panitumumab-IRDye800 half-life (14.5 h – 24.8 h in the 0.06 – 1.5 mg/kg dose range (*21*)), body weight and imaging window can influence the antibody plasma concentration and contribute to the variance in fluorescence. Therefore, antibody concentration in individual tissue types were normalized by corresponding day-of-surgery plasma

concentration. Moreover, fluorescence signal was normalized by autofluorescence to mitigate variability in tissue section thickness (< 2% (*22*)) and corrected for overestimation of antibody concentration (12.9%) due to shrinkage from tissue processing (11.4% (*23*)). Variable dye-to-protein ratios across production batches, photo bleaching and metabolic rates can introduce noise and bias in methods using fluorescence as surrogate for antibody presence. Thus our fluorescence-based results are yet to be validated and calibrated by direct antibody quantification techniques such as mass spectrometry. Additional tissue properties including collagen, stromal and immune markers in the tumor microenvironment may also account for differential fluorescence intensity, which can be investigated in future studies.

CONCLUSION

Cellular EGFR expression, tumor cell density, plasma antibody concentration and delivery barrier determined fluorescent antibody distribution in tissue, which differentially translated to macroscopic tumor contrast depending on tumor size, tumor depth and intraoperative imaging conditions in HGG, HNSCC and LAC patients infused with a NIR-labeled EGFR antibody. Potential clinical utilities of molecular targeted fluorescence imaging include intraoperative real-time tumor visualization, pathological margin detection and antibody distribution projection, with implication for oncologically sound resections, informed decision-making on therapy and regulatory approval of new imaging probes that has the potential to transform standard-of-care practice and patient care.

ACKNOWLEDGMENTS

This work was supported in part by the Stanford Comprehensive Cancer Center, the Stanford University School of Medicine Medical Scholars Program, the Netherlands Organization for Scientific Research (Rubicon; 019.171LW.022), the National Institutes of Health and the National Cancer Institute (R01CA190306), National Institute on Deafness and Other Communication Disorders (T32DC015209), a scientific research grant from the Yokoyama Foundation for Clinical Pharmacology (YRY-1702), and an institutional equipment loan from LI-COR Biosciences Inc. Illustrations were created with BioRender.

KEY POINTS

Question

What physical imaging conditions and biological tissue properties contributed to the differential translation of biomarker expression to clinical imaging outcomes in fluorescence-guided surgery?

Pertinent Findings

In brain, head-and-neck and lung cancer patients, cellular EGFR expression, tumor cell density, plasma antibody concentration and delivery barrier predicted the heterogeneous intratumoral antibody distribution, while open-field imaging device setting, lighting conditions, tumor size and depth substantially influenced the macroscopic fluorescence contrast.

Implications for Patient Care

By bridging the gap between molecular characteristics and imaging outcome, appropriate qualities of tumor biology and acquisition settings for optimal clinical implementation of targeted fluorescence imaging may facilitate assessment and adoption of emerging theranostic imaging probes.

REFERENCES

1. Gao RW, Teraphongphom NT, van den Berg NS, et al. Determination of tumor margins with surgical specimen mapping using near-infrared fluorescence. *Cancer Res.* 2018;78:5144-5154.

2. Zhou Q, van den Berg NS, Rosenthal EL, et al. EGFR-targeted intraoperative fluorescence imaging detects high-grade glioma with panitumumab-IRDye800 in a phase 1 clinical trial. *Theranostics.* 2021;11:7130-7143.

3. Tanyi JL, Chon HS, Morgan MA, et al. Phase 3, randomized, single-dose, open-label study to investigate the safety and efficacy of pafolacianine sodium injection (OTL38) for intraoperative imaging of folate receptor positive ovarian cancer. *J Clin Oncol.* 2021;39:5503-5503.

4. Hoogstins CE, Boogerd LS, Mulder BGS, et al. Image-guided surgery in patients with pancreatic cancer: first results of a clinical trial using SGM-101, a novel carcinoembryonic antigen-targeting, near-infrared fluorescent agent. *Ann Surg Oncol.* 2018;25:3350-3357.

5. Hekman MC, Rijpkema M, Muselaers CH, et al. Tumor-targeted dual-modality imaging to improve intraoperative visualization of clear cell renal cell carcinoma: a first in man study. *Theranostics.* 2018;8:2161.

6. Schottelius M, Wurzer A, Wissmiller K, et al. Synthesis and preclinical characterization of the PSMA-targeted hybrid tracer PSMA-I&F for nuclear and fluorescence imaging of prostate cancer. *J Nucl Med.* 2019;60:71-78.

7. Boogerd LS, Hoogstins CE, Schaap DP, et al. Safety and effectiveness of SGM-101, a fluorescent antibody targeting carcinoembryonic antigen, for intraoperative detection of colorectal cancer: a dose-escalation pilot study. *Lancet Gastroenterol Hepatol.* 2018;3:181-191.

8. Koller M, Qiu S-Q, Linssen MD, et al. Implementation and benchmarking of a novel analytical framework to clinically evaluate tumor-specific fluorescent tracers. *Nat Commun.* 2018;9:1-11.

9. Schneider CA, Rasband WS, Eliceiri KW. NIH Image to ImageJ: 25 years of image analysis. *Nat Methods.* 2012;9:671-675.

10. Van Keulen S, Nishio N, Birkeland A, et al. The sentinel margin: intraoperative ex vivo specimen mapping using relative fluorescence intensity. *Clin Cancer Res.* 2019;25:4656-4662.

11. Mehner C, Oberg AL, Goergen KM, et al. EGFR as a prognostic biomarker and therapeutic target in ovarian cancer: evaluation of patient cohort and literature review. *Genes Cancer.* 2017;8:589.

12. van Keulen S, Nishio N, Fakurnejad S, et al. Intraoperative tumor assessment using real-time molecular imaging in head and neck cancer patients. *J Am Coll Surg.* 2019;229:560-567.e1.

13. Nishio N, van Keulen S, van den Berg NS, et al. Probe‐based fluorescence dosimetry of an antibody‐dye conjugate to identify head and neck cancer as a first step to fluorescence‐guided tissue preselection for pathological assessment. *Head Neck.* 2020;42:59-66.

14. van Keulen S, van den Berg NS, Nishio N, et al. Rapid, non-invasive fluorescence margin assessment: optical specimen mapping in oral squamous cell carcinoma. *Oral Oncol.* 2019;88:58-65.

15. Lu G, Fakurnejad S, Martin BA, et al. Predicting therapeutic antibody delivery into human head and neck cancers. *Clin Cancer Res.* 2020.

16. Uhlen M, Zhang C, Lee S, et al. A pathology atlas of the human cancer transcriptome. *Science.* 2017;357:eaan2507.

17. Zhou Q, Leonel JCV, Santoso MR, et al. Molecular imaging of a fluorescent antibody against epidermal growth factor receptor detects high-grade glioma. *Sci Rep.* 2021;11:1-12.

18. Tummers WS, Miller SE, Teraphongphom NT, et al. Intraoperative pancreatic cancer detection using tumor-specific multimodality molecular imaging. *Ann Surg Oncol.* 2018:1-9.

19. de Boer E, Warram JM, Tucker MD, et al. In vivo fluorescence immunohistochemistry: localization of fluorescently labeled cetuximab in squamous cell carcinomas. *Sci Rep.* 2015;5:1-11.

20. Zhou Q, Li G. Fluorescence-guided craniotomy of glioblastoma using panitumumab-IRDye800. *Neurosurg Focus Video.* 2022;6:V9.

21. Pei J, Juniper G, van den Berg NS, et al. Safety and stability of antibody-dye conjugate in optical molecular imaging. *Mol Imaging Biol.* 2020:1-8.

22. Matenaers C, Popper B, Rieger A, Wanke R, Blutke A. Practicable methods for histological section thickness measurement in quantitative stereological analyses. *PLoS One.* 2018;13:e0192879.

23. Tran T, Sundaram CP, Bahler CD, et al. Correcting the shrinkage effects of formalin fixation and tissue processing for renal tumors: toward standardization of pathological reporting of tumor size. *J Cancer.* 2015;6:759.

Table. 1 Patient characteristics

	HGG (n = 5)	HNSCC (n = 23)	LAC (n = 3)	Total (n = 31)	*P* value
Age, y (median/range)	62 (42-72)	67 (44-82)	71 (67-71)	67 (42-82)	0.41[a]
Gender, Male (%)	2 (40%)	10 (43%)	1 (33%)	13 (42%)	0.94[b]
Race					0.31[b]
Asian	1 (20%)	2 (9%)	1 (33%)	4 (13%)	
White	4 (80%)	20 (87%)	2 (67%)	26 (84%)	
Unknown/Not reported	0 (0%)	1 (4%)	0 (0%)	1 (3%)	
Tumor size, cm (median/range)	5.0 (3.5-6.1)	2.8 (1.0-9.0)	2.3 (1.9-3.5)	3.7 (1.0-9.0)	0.35[a]
Pan800 dose, mg/kg (mean ± SD)	0.8 ± 0.3	0.8 ± 0.2	0.6 ± 0.3	0.7 ± 0.2	0.84[a]
Pan800 DOS plasma conc., mg/L (mean± SD)	6.9 ± 3.5	5.5 ± 4.2	3.9 ± 3.7	5.5 ± 4.0	0.58[a]
Imaging window, days, (median/range)	1.8 (0.6-2.9)	1.8 (0.8-3.8)	1.7 (0.9-1.8)	1.8 (0.6-3.8)	0.95[a]

[a] One-way AVOVA; [b] Pearson's chi-squared test; HGG: high-grade glioma; HNSCC: head-and-neck squamous cell carcinoma; LAC: lung adenocarcinoma; Pan800, panitumumab-IRDye800; DOS: day of surgery.

1 Table 2 Results of multivariate linear regression analysis

Variable	β (95% CI)	*P* value
Tumor cell density	0.001447 (0.0002783, 0.002616)	0.0154
Cellular EGFR expression%	0.02561 (0.009501, 0.04171)	0.0019
Pan800 plasma concentration	4.498 (4.01, 4.986)	< 0.0001
Delivery barrier [No]	2.119 (1.376, 2.861)	< 0.0001

β, regression coefficient; CI, confidence interval; EGFR, epidermal growth factor receptor; Pan800, panitumumab-IRDye800

2

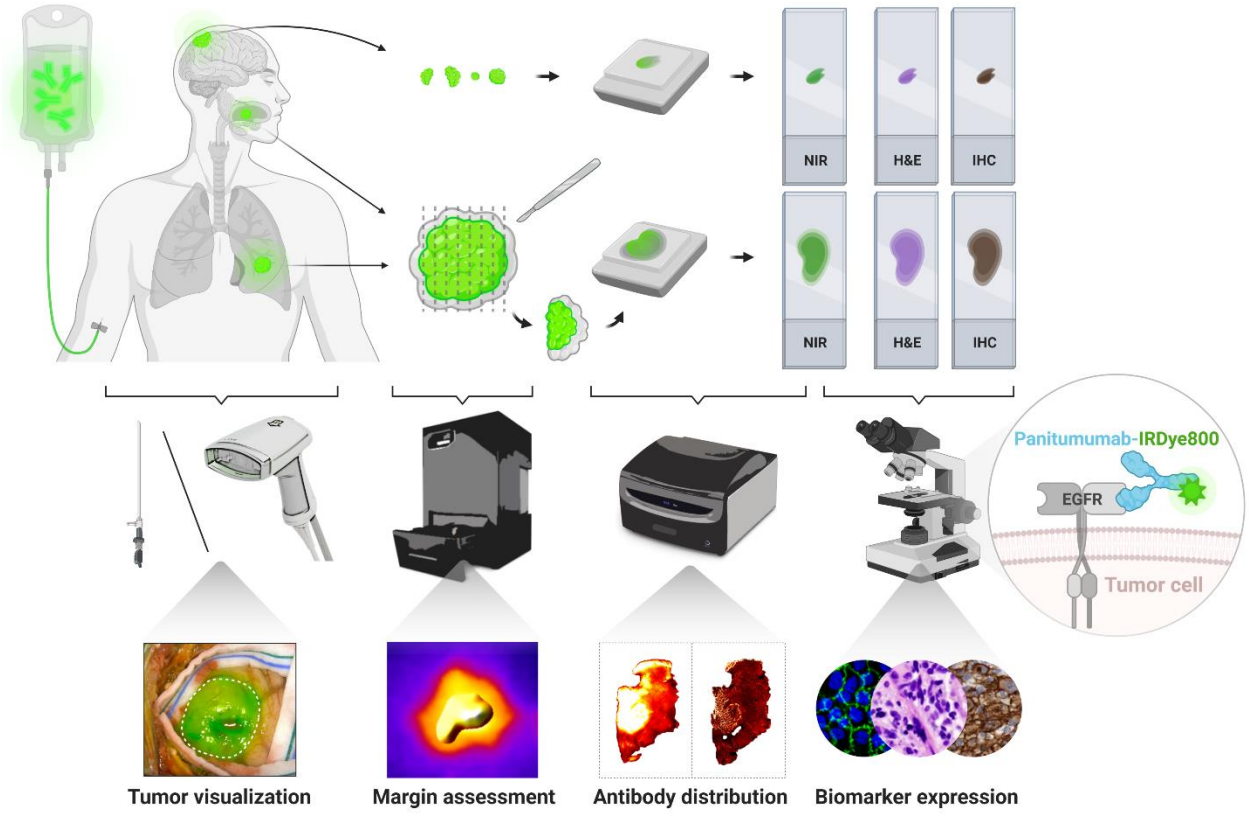

Figure 1. Tissue processing and imaging workflow.

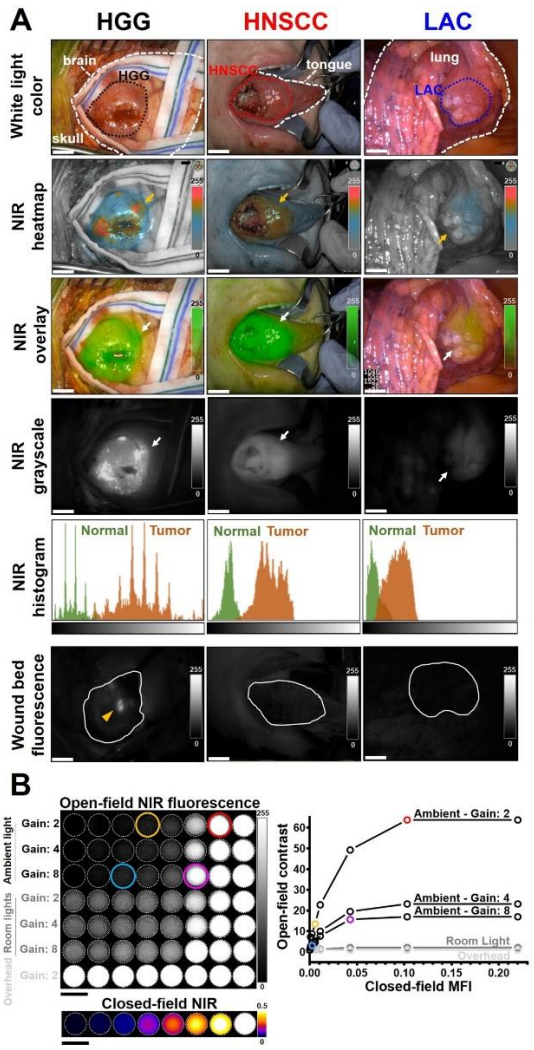

Figure 2. Intraoperative NIR fluorescence imaging enhanced tumor contrast *in vivo*. (A) Representative annotated (*dashed lines*) white light photographs and fluorescence images of exposed tumors (*dotted outlines*) and wound beds (*solid outlines*) in the surgical field. HGG: high-grade glioma; HNSCC: head-and-neck squamous carcinoma; LAC: lung adenocarcinoma; NIR: near-infrared; *Arrows*: positive NIR fluorescence signal; *Arrowhead*: residual tumor; Histogram (of NIR grayscale images) *X-axis*: pixel fluorescence intensity (range: 0 – 255), *Y-axis*: pixel count (range: 0 – 5000). Scale bars = 1 cm. (B) NIR fluorescence images of tissue-mimicking phantoms containing serial dilutions of panitumumab-IRDye800 (0 – 10 μg/mL) acquired in either an open-field imager under three lighting conditions with various gain settings, or a closed-field device. MFI: mean fluorescence intensity; Scale bars = 1 cm.

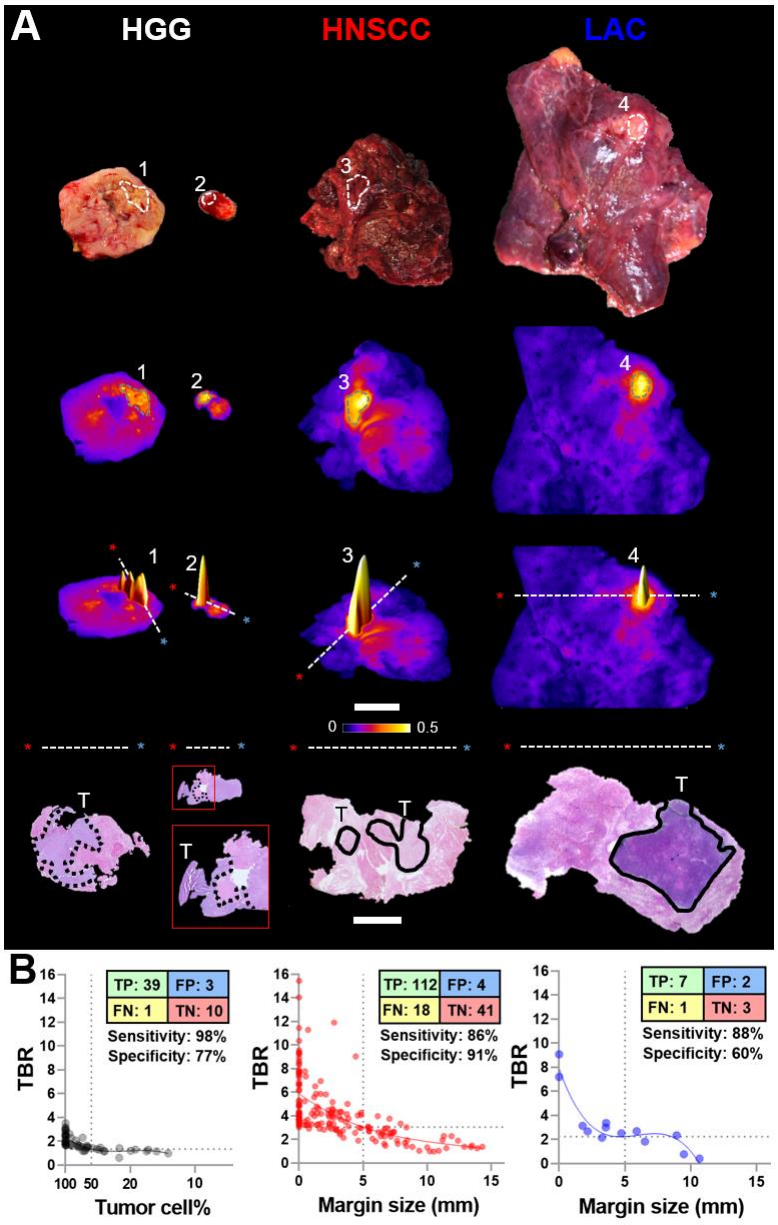

Figure 3. Macroscopic closed-field NIR imaging identified at-risk margins in resected tissue. (A) Representative intraoperative photographs and fluorescence images of resected tissue specimens (1 – 4: fluorescence intensity peaks). Scale bar = 2 cm. The *dashed lines* and *asterisks* (*red & blue*) indicate the orientation in which histology (hematoxylin and eosin) slides with infiltrative (*dotted outlines*) and solid (*solid outlines*) tumors (T) were sectioned. Scale bar = 1 cm. (B) Fluorescence target-to-background ratio (TBR) correlated with tumor cell percentage (HGG) and margin size (HNSCC and LAC), respectively. TP: true positive; FP: false positive; TN: true negative; FN: false negative.

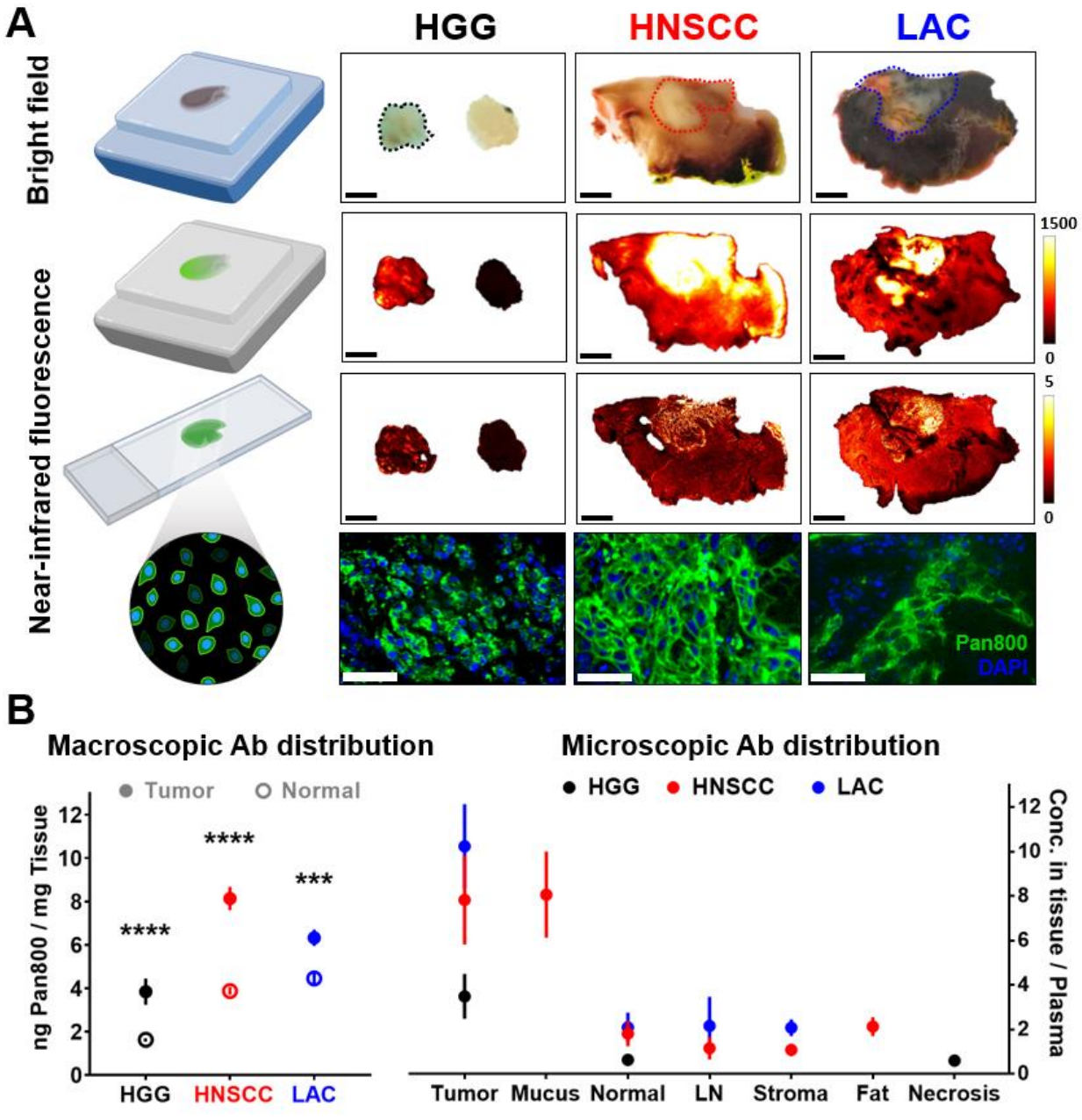

Figure 4. Intratumoral distribution and cellular delivery of fluorescent antibody. (A) Bright field photographs (scale bars = 5 mm; *dotted outlines*: tumor) and fluorescence images (scale bars = 50 μm) of fixed tissue blocks and sections. (B) Macroscopic and microscopic distribution of panitumumab-IRDye800 in histological tissue types.

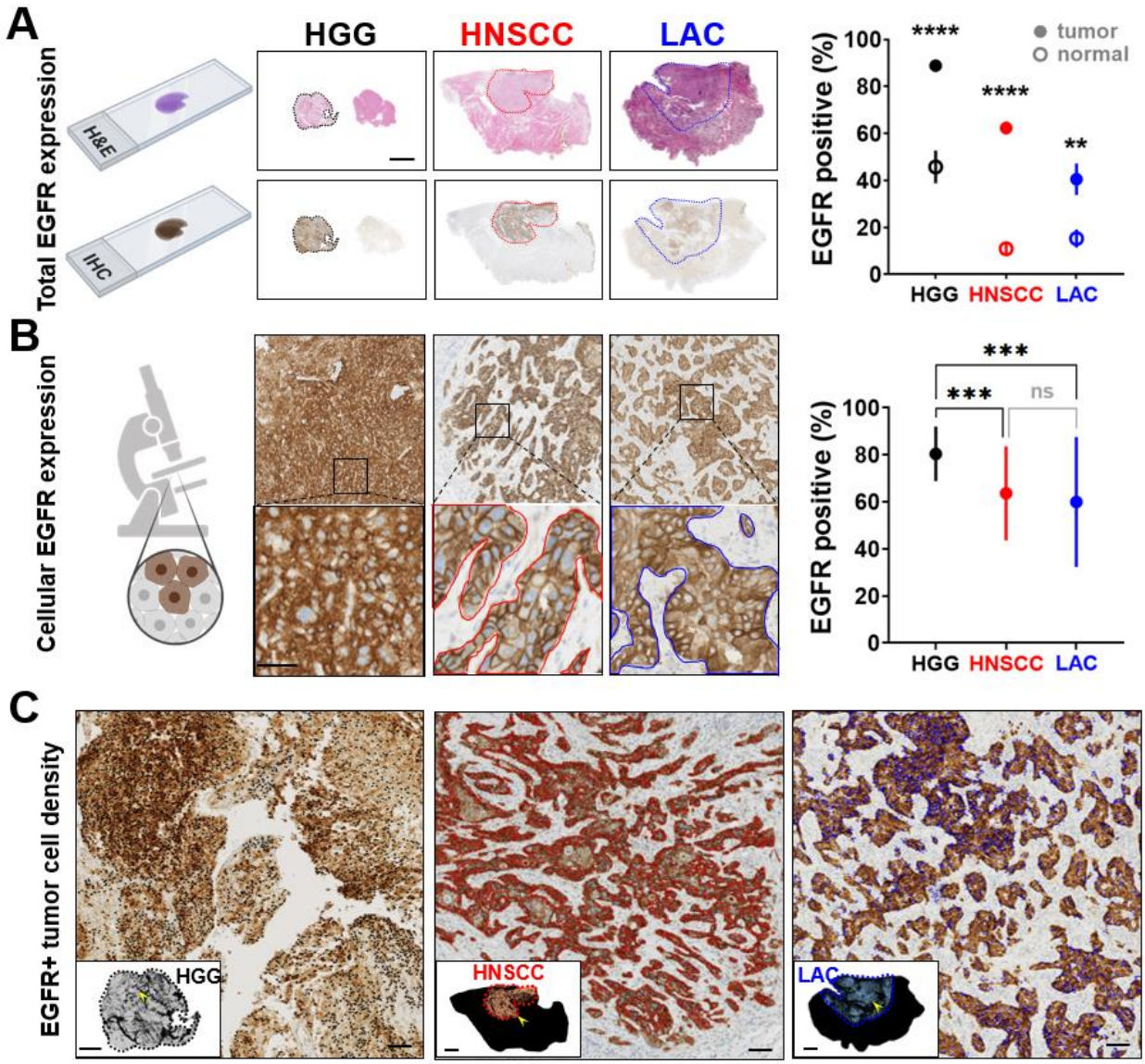

Figure 5. Heterogeneous EGFR expression in tumor. Tumor areas (scale bar = 5 mm; *dotted outlines*) on tissue sections of histological (hematoxylin and eosin) and EGFR immunohistochemical stainings with (A) total and (B) cellular EGFR expression (scale bar = 50 μm; *solid outlines*). (C) EGFR+ tumor cells (*black*: HGG; *red*: HNSCC; *blue*: LAC; scale bars = 200 μm) within tumor areas. *Insets*: distribution of EGFR+ tumor cells on whole tissue sections (scale bar = 2 mm (HGG); scale bars = 2 cm (HNSCC and LAC)); *Arrowheads*: location of high magnification microscopic views.

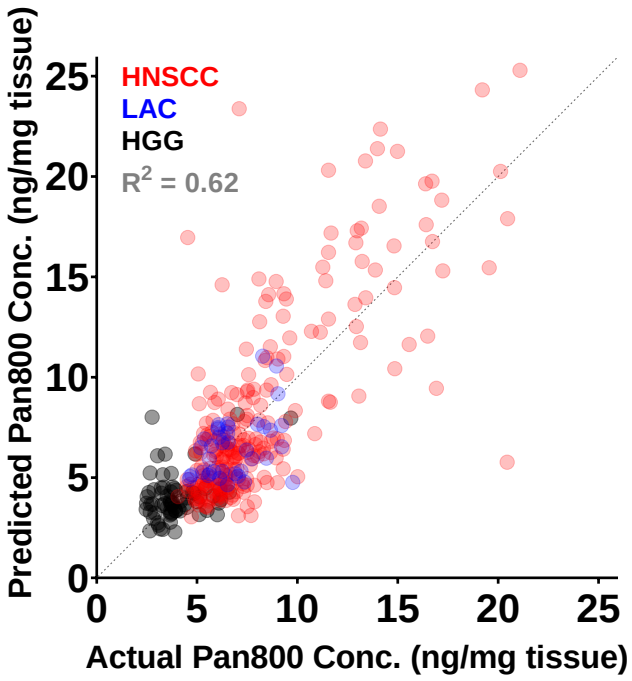

Figure 6. Goodness-of-fit for predicting local panitumumab-IRDye800 concentration from four biological factors in a multiple regression model across three cancers.

Graphical Abstract

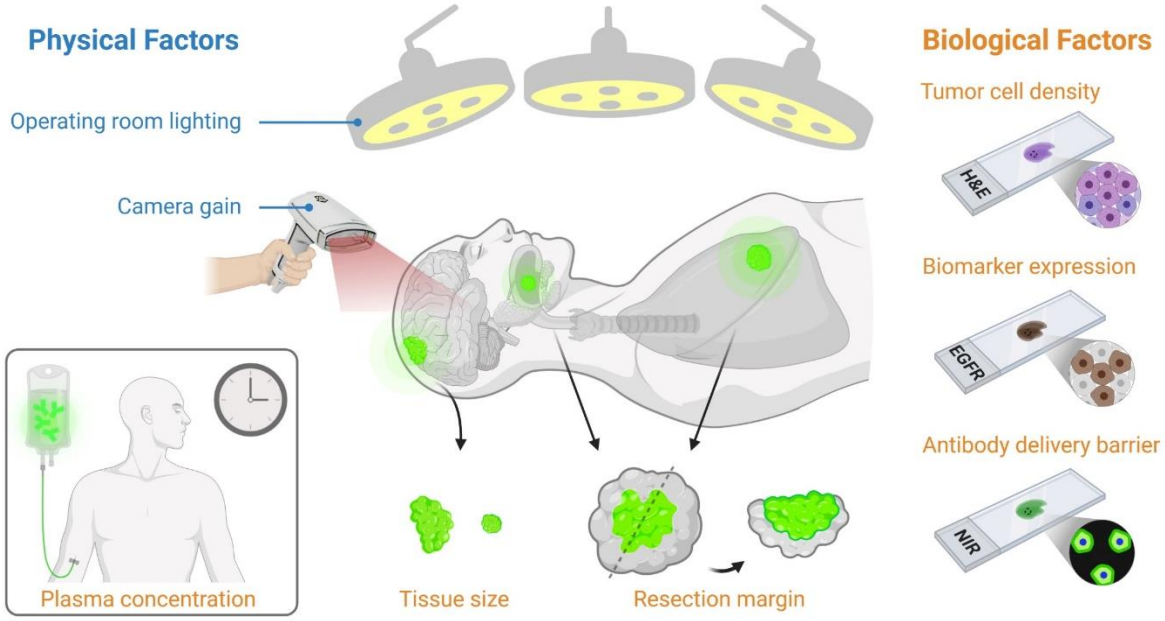

Supplementary Information

Supplementary Table S1. Number of adverse events recorded within 30 days of panitumumab-IRDye800 infusion in three cancer types.

	HGG (n = 5)	**HNSCC** (n = 23)	**LAC** (n = 3)	**Total** (n = 31)
Infusion reactions	No	No	No	No
Total serious adverse events	0	0	0	0
Total non-serious adverse events (mean ± SD)	8 (1.75 ± 2.22)	46 (2.09 ± 1.85)	4 (1.33 ± 1.15)	58 (1.97 ± 1.80)
Grade I	6	35	3	44
Grade II	2	8	1	11
Grade III	0	3	0	3
Attribution	Unrelated	Unrelated	Unrelated	Unrelated
Dose limiting toxicity	No	No	No	No

Supplementary Figure S1 Fresh resected tumor tissue size from three trials. *** $P = 0.0001$ by ANOVA.

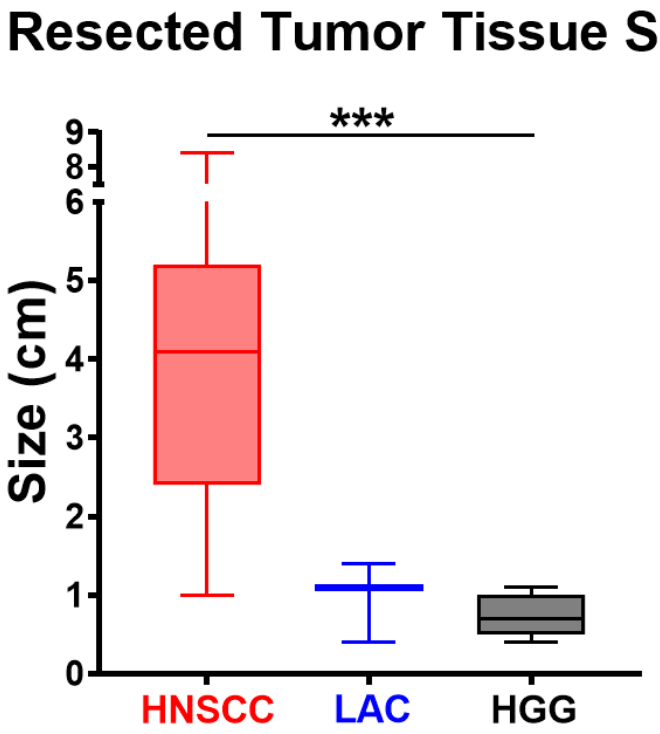

Supplementary Figure S2 Neuronavigation identified the location (*asterisk*) of residual tumor in the wound bed on presurgical MR images, where language cortex involvement was indicated on fMRI mapping. P*ink*: visual responsive naming; *red*: object naming; *cyan*: auditory responsive naming; *blue*: negative BOLD signal; *grayscale*: preoperative T1-weighted imaging; *glow*: T1 contrast enhancement.

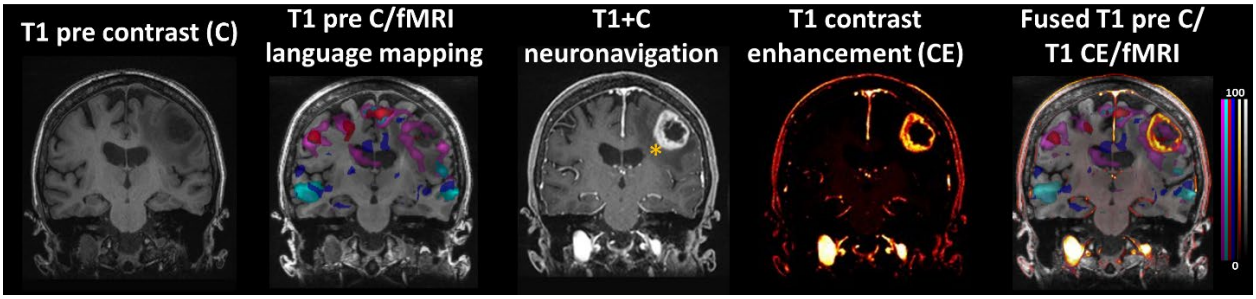

Supplementary Figure S3 Intraoperative target-to-background ratio (TBR) of tumor under white light and NIR illumination, versus fluorescent contrast of wound beds.

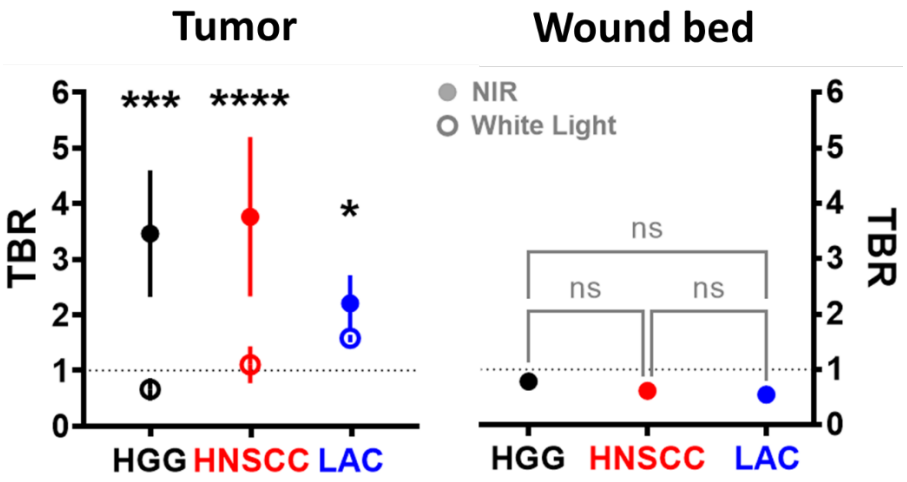

Supplementary Figure S4 Correlation of fresh tumor tissue size with corresponding NIR target-to-background ratio (TBR). Each symbol represents one patient. Linear regression lines are fitted for each cancer type as well as for all patients combined.

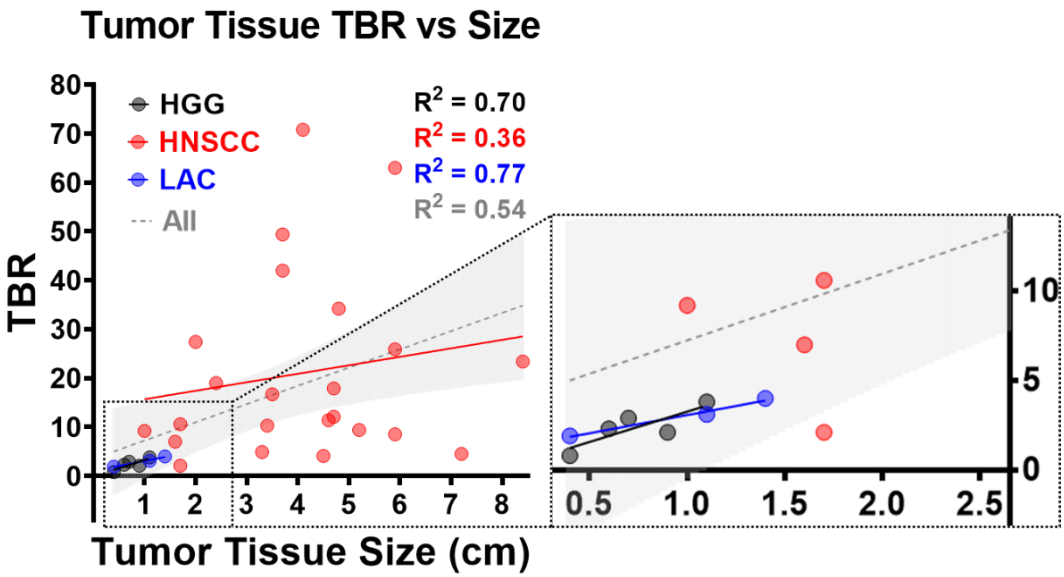

Supplementary Figure S5 NIR heterogeneity and tumor contrast in tissue sections

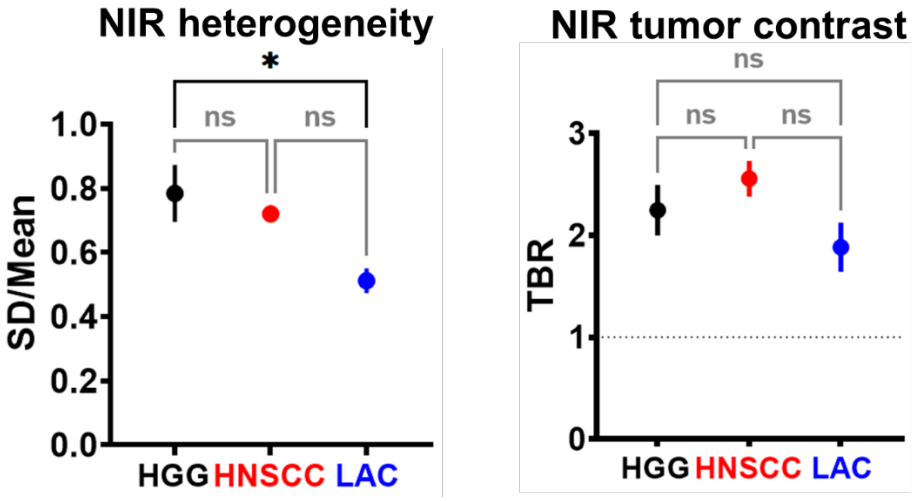

Supplementary Figure S6 Receiver operating characteristic curves and corresponding diagnostic performance characteristics of tissue section NIR fluorescence for tumor detection. Diagnostic performance characteristics of tissue section NIR fluorescence for tumor detection, including sensitivity (Sen.), specificity (Spe.), positive predictive value (PPV), negative predictive value (NPV) area under the curve (AUC), and MFI cutoff values for maximal sensitivity and specificity combined.

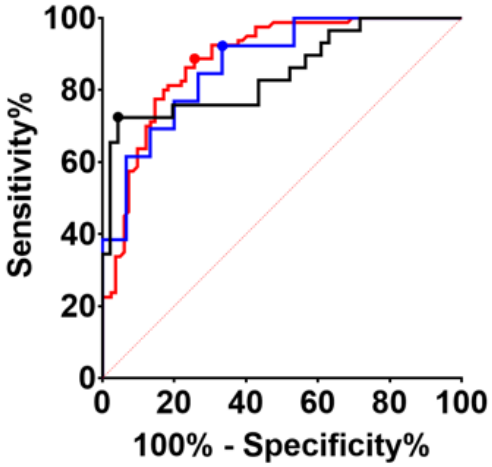

	HGG	HNSCC	LAC
Sensitivity	72%	89%	92%
Specificity	96%	74%	67%
PPV	91%	77%	71%
NPV	85%	87%	91%
AUC	0.85	0.89	0.87
MFI cutoff	0.55	0.74	0.98

Supplementary Figure S7 *Ex vivo* MFI by tissue type. Mean fluorescence intensity of fresh resected tumor (T) and normal (N) tissue (from left to right: $P < 0.0001$, $P = 0.2$, $P = 0.04$, $P = 0.08$), formalin fixed paraffin embedded tissue blocks (from left to right: $P < 0.0001$, $P < 0.0001$, $P = 0.25$, $P = 0.05$), and 4μm-thick tissue sections (from left to right: $P < 0.0001$, $P = 0.001$, $P = 0.6$, $P < 0.0001$). Paired t-test was performed for group comparisons.

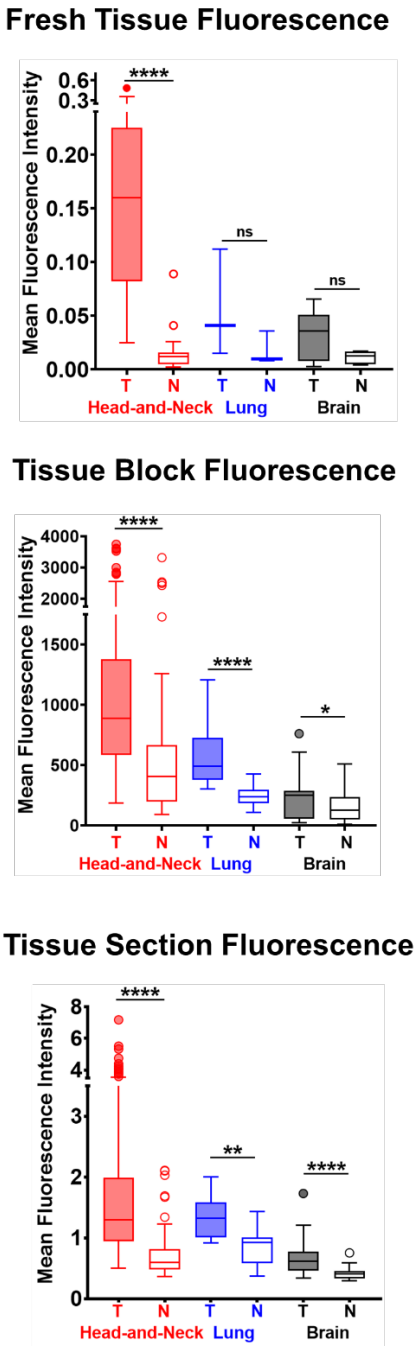

Supplementary Figure S8 An array of phantoms imaged with two closed-field devices (*top*: Pearl Trilogy Imager; *bottom*: Odyssey CLx Flatbed Imager). Correlation of mean fluorescence intensities measured in each phantom between the two instruments. Each symbol is the average of three replicate measurements. Third order (cubic) polynomial least square curve fitting was performed.

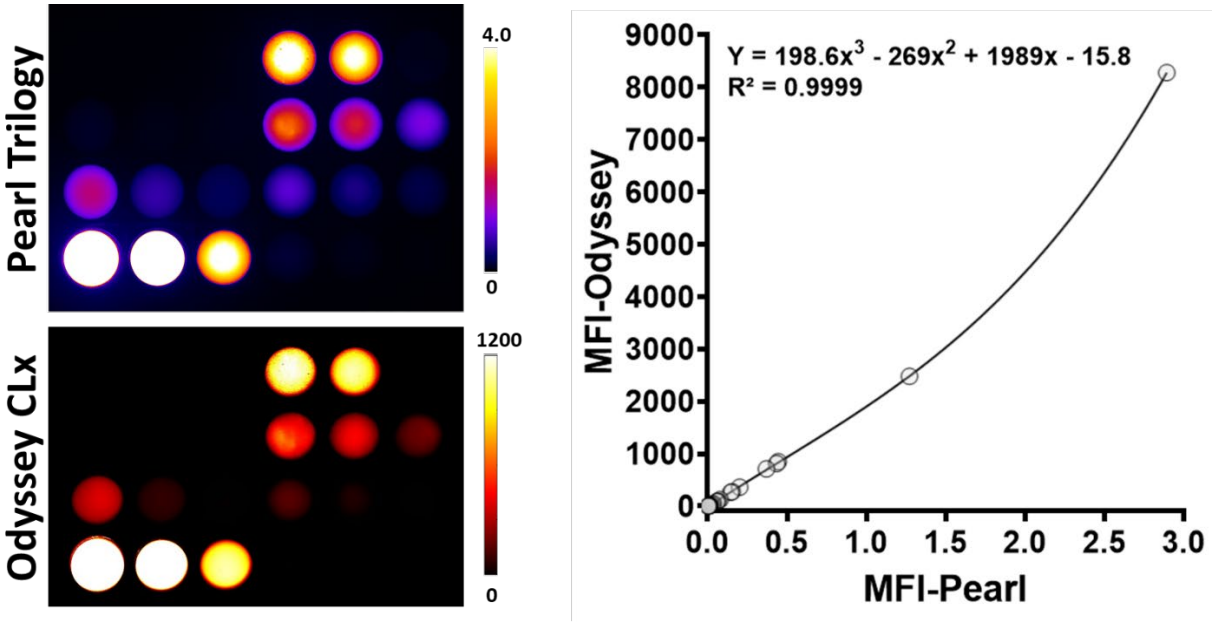

Supplementary Figure S9 Standard curves of panitumumab-IRDye800 concentration versus mean fluorescence intensity in phantoms. Each symbol is the average of three replicate measurements. Third order (cubic) polynomial least square curve fitting were performed in the concentration ranges of 0 – 1 μg/mL and 1 – 10 μg/mL, respectively.

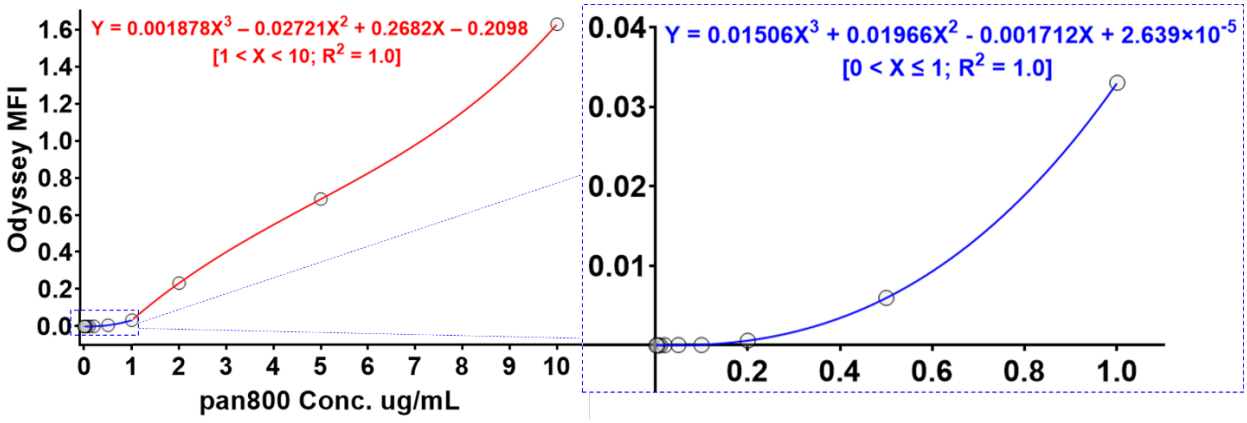

Supplementary Figure S10 EGFR expression as a biomarker for tumor on whole tissue sections. Performance was compared among three cancer types in terms of sensitivity (Sen.), specificity (Spe.), positive predictive value (PPV), negative predictive value (NPV), area under the curve (AUC) and EGFR+% cutoff values for maximal sensitivity and specificity combined.

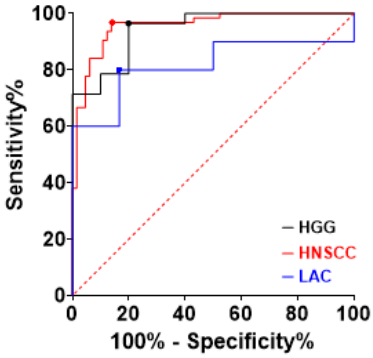

	HGG	HNSCC	LAC
Sensitivity	96%	97%	80%
Specificity	80%	86%	83%
PPV	93%	87%	80%
NPV	89%	97%	83%
AUC	0.94	0.96	0.82
EGFR+% cutoff	66.71	17.63	29.65

HGG: high-grade glioma; HNSCC: head-and-neck squamous cell carcinoma; LAC: lung adenocarcinoma; PPV: positive predictive value; NPV: negative predictive value; AUC: area under the curve; EGFR: epidermal growth factor receptor

Supplementary Figure S11 Double immunohistochemical staining of Claudin-5 (tight-junction protein, *brown*) and ETS-related gene (ERG, endothelial nucleus, *magenta*) on representative brain specimen containing normal brain and HGG tissue. *Arrows*: blood vessels; *dotted line*: infiltration edge.

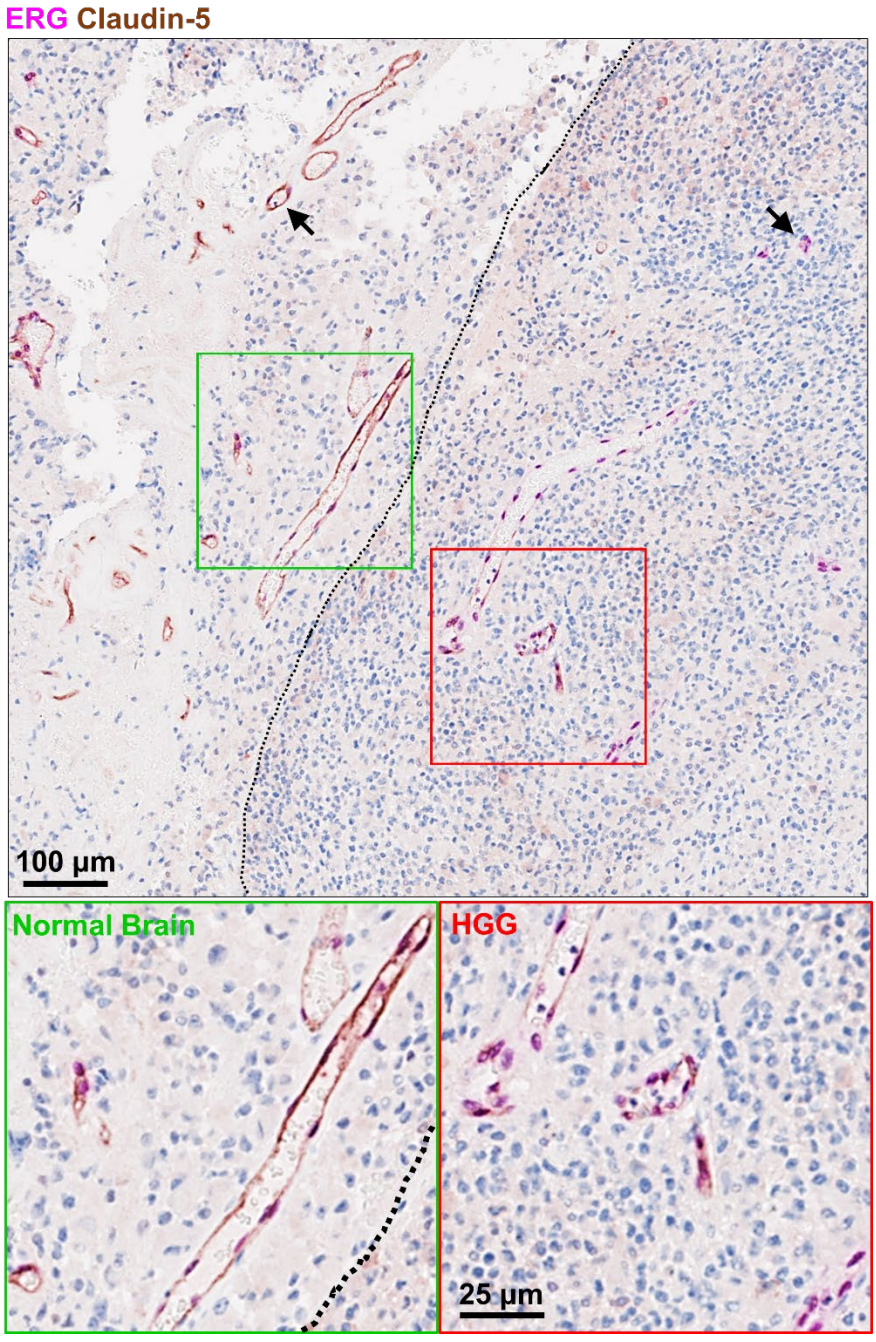

Supplementary Figure S12 Tumor cell density and distribution in three cancer types. Histograms of percentage of tumor area occupied by a certain number of tumor cells per mm^2 in HGG, HNSCC and LAC.

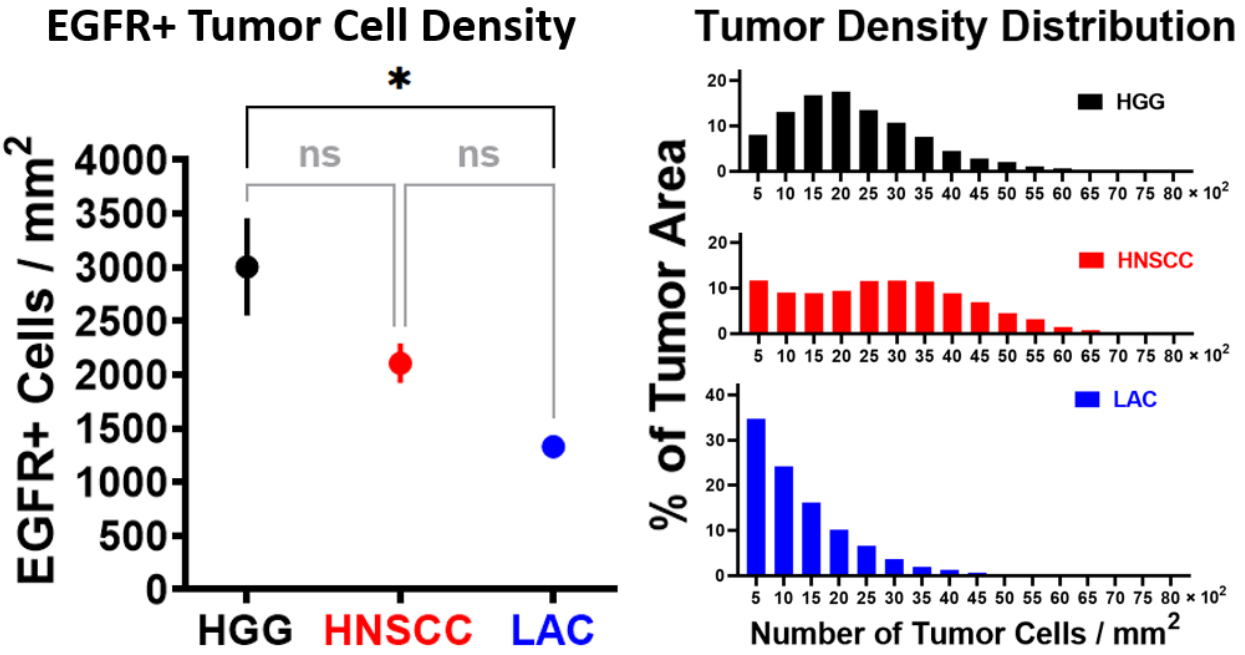

Supplementary Figure S13 Immunohistochemical EGFR staining intensity quantification. Immunohistochemical staining intensity heatmaps of total tumoral EGFR, histograms (tumor vs. normal), intratumoral EGFR and cellular EGFR expression (*red*: strong positive; *orange*: medium positive; *yellow*: weak positive; *blue*: negative) in three cancer types. *Solid outlines*: tumor; *arrows*: areas of positive EGFR expression magnified in the 2nd column.